INSTITUT NATIONAL DE RECHERCHE EN INFORMATIQUE ET EN AUTOMATIQUE

Identification robuste de sillages tourbillonnaires controllés

Jessie Weller — Edoardo Lombardi — Angelo Iollo

N° 6559

Juin 2008

Thème NUM

Rapport de recherche

ISSN 0249-6399 ISRN INRIA/RR--6559--FR+ENG

Identification robuste de sillages tourbillonnaires controllés

Jessie Weller* , Edoardo Lombardi* , Angelo Iollo*

Thème NUM — Systèmes numériques
Équipe-Projet MC2

Rapport de recherche n° 6559 — Juin 2008 —23 pages

Résumé : Nous proposons une méthode de réduction de modèle, pour des écoulements actionnés, basée sur la régularisation d'un problème inverse. Le problème inverse vise à minimiser l'erreur entre les prédictions du modèle et des simulations de référence. Les paramètres à identifier sont les coefficients d'une expansion polynomiale qui modélise les dynamiques temporelles d'un nombre limité de modes globales. Ces modes sont obtenus par Décomposition Orthogonale aux valeurs Propres (POD). Il s'agit d'une méthode pour calculer les éléments les plus représentatifs, en termes d'énergie, d'une base de données de simulations. Il est montré que des modèles basés sur une simple projection de Galerkin et sur des techniques classiques de calibration ne sont pas viables. Ils sont soit mal posés, soit donnent une approximation erronée de la solution dès qu'ils sont utilisés pour prédire des dynamiques n'appartenant pas à la base de données originale. En revanche, des évidences numériques montrent que la méthode que nous proposons permet de construire des modèles robustes, qui réagissent correctement à des variations de paramètres, et pourraient donc tre utilisés pour des problèmes de contrôle d'écoulement.

Mots-clés : modèles réduits, contrôle, problèmes inverses

* IMB - Université Bordeaux et MC2 - INRIA Bordeaux Sud-Ouest, 33405 Talence, France

Centre de recherche INRIA Bordeaux – Sud Ouest
Domaine Universitaire - 351, cours de la Libération 33405 Talence Cedex
Téléphone : +33 5 40 00 69 00

Robust model identification of actuated vortex wakes

Abstract: We present a low-order modeling technique for actuated flows based on the regularization of an inverse problem. The inverse problem aims at minimizing the error between the model predictions and some reference simulations. The parameters to be identified are a subset of the coefficients of a polynomial expansion which models the temporal dynamics of a small number of global modes. These global modes are found by Proper Orthogonal Decomposition, which is a method to compute the most representative elements of an existing simulation database in terms of energy. It is shown that low-order control models based on a simple Galerkin projection and usual calibration techniques are not viable. They are either ill-posed or they give a poor approximation of the solution as soon as they are used to predict cases not belonging to the original solution database. In contrast, numerical evidence shows that the method we propose is robust with respect to variations of the control laws applied, thus allowing the actual use of such models for control.

Key-words: reduced order models, control, inverse problems

1 Introduction

We consider the problem of describing the dynamics of an infinite dimensional system using a small number of degrees of freedom. In particular we concentrate on the problem of devising accurate and robust models of actuated fluid flows past bluff obstacles. These flows are dominated by the presence of large-scale vortices due to massive separation, and are good candidates for a low-dimensional representation. The point of view that we privilege is empiric : the functional space in which we seek the low-dimensional solution is derived using proper orthogonal decomposition (POD) [16]. POD makes use of simulation databases to determine optimal functional spaces in terms of solution representation. A vast literature concerning this way of modeling fluid flows exists [8, 4, 9, 17], and some results show the possible interest of using POD in applications such as flow control [2, 10, 11].
However, several problems related to the idea of modeling a flow by a small number of variables are open. One of the issues is the asymptotic stability of the models obtained. Often such models are capable of correctly reproducing the dynamics over small time intervals, whereas the asymptotic behavior converges to incorrect limit cycles [17]. This issue is related to both numerical artifacts and to an improper representation of the solution [15, 20, 18]. As a results low-order models are of delicate use and not robust to parameter variations.
The present study describes a method to obtain robust low-order models. In previous works we showed that it is possible to obtain accurate low-order models of relatively complicated flows by minimizing the error between the model results and the reference solution [4]. Here we extend those works to cases where the flow is actuated by devices that can affect locally or globally the velocity and pressure fields. The objective is to derive a low-order model that provides accurate predictions and that is robust to variations of the control law employed. The main idea is to identify the manifold over which the non-linear dynamics of the POD modes lies, when the input to the system is varied. In this spirit, several dynamics are included in the identification procedure coupled with a Tikhonov type regularization. The case of a precomputed control as well as the case of a feed-back control are studied.
The practical relevance of this work is that low-order models make possible to devise or to optimize controls for large-scale problems that would not be otherwise solvable in terms of computational size. Applications of this method is straight forward for models other than the Navier-Stokes equations.

2 Reduced Order Modeling using POD

2.1 Flow setup

We consider a two-dimensional laminar flow past a confined square cylinder. This setup presents a reasonable compromise between physical complexity and computational cost. A sketch showing the geometry, the frame of reference and the adopted notation is plotted in Fig.1. At the inlet, the incoming flow is assumed to have a Poiseuille profile with maximum center-line velocity U. With reference to Fig.1, $L/H = 1/8$,

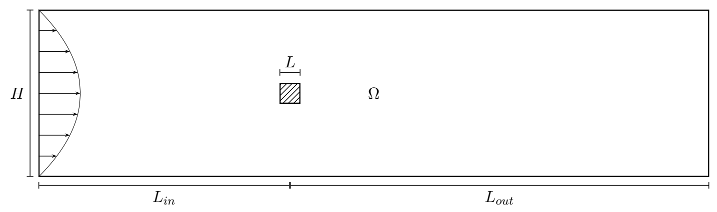

FIG. 1 – Computational domain Ω.

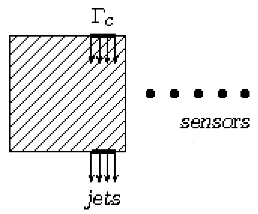

FIG. 2 – Placement of synthetic jet and sensors for control

$L_{in}/L = 12$, $L_{out}/L = 20$. No-slip conditions are enforced both on the cylinder and on the parallel walls. Details concerning the grids and the numerical set up are reported in [4].
All the quantities mentioned in the following have been made non-dimensional by L and U. The two-dimensional unforced flow obtained is a classic vortex street with a well defined shedding frequency. The interaction with the confining walls leads to some peculiar features, like the fact that the vertical position of the span-wise vortices is opposite to the one in the classic von Kármán street [6].
The presence of an actuator is modeled by imposing a new boundary condition on a small surface Γ_c of $\partial\Omega$:

$$\boldsymbol{u}(\boldsymbol{x},t)\cdot\boldsymbol{n}(\boldsymbol{x}) = c(t), \quad \boldsymbol{x}\in\Gamma_c$$

For control purposes we place two actuators on the cylinder. They are driven in opposite phase, as shown in Fig. 2 :

$$v(\boldsymbol{x},t) = c(t), \quad \boldsymbol{x}\in\Gamma_c$$

The control law $c(t)$ can be precomputed, or obtained using a proportional feedback law. For example, using measurements of the vertical velocity at points $\boldsymbol{x}_j$ in the cylinder wake, we can define a proportional control law :

$$c(t) = \sum_{j=1}^{N_s} \mathsf{K}_j v(\boldsymbol{x}_j, t)$$

where N_s denotes the number of sensors used.

2.2 Proper Orthogonal decomposition with the snapshot method

Seeking a reduced order solution that can be written

$$\boldsymbol{u}_R(\boldsymbol{x},t) = \sum_{r=1}^{N_r} a_r(t)\boldsymbol{\Phi}^r(\boldsymbol{x})$$

where the spatial functions $\boldsymbol{\Phi}^r$ are obtained by POD has become a popular approach when dealing with large scale systems. A vast literature concerning the POD procedure exists [14], we refer to these works for a more general review of the method.

2.2.1 The POD basis

In our case, a numerical simulation of the Navier-Stokes equations is performed over a time interval $[0,T]$, and the velocity field is saved at N_t time instants $t_i \in [0,T]$. This yields a data set $\{\boldsymbol{u}^i(\boldsymbol{x}) = \boldsymbol{u}(\boldsymbol{x},t^i)\}_{i=1..N_t}$. The aim of the POD procedure is to find a low dimensional subspace of $\mathcal{L} = span\{\boldsymbol{u}^1,\cdots,\boldsymbol{u}^{N_t}\}$, that gives the best approximation of $\mathcal{L}$. We therefore seek an orthonormal set $\{\boldsymbol{\Phi}^r\}_{r=1...N_r}$, where $N_r << N_t$, and a set of coefficients $\hat{a}^i_k$ such that the reconstruction error :

$$\sum_{i=1}^{N_t}\left\|\boldsymbol{u}^i - \sum_{r=1}^{N_r}\hat{a}^i_k\boldsymbol{\Phi}^r\right\|^2_{L^2(\Omega)} \tag{1}$$

is minimal.
Following Sirovich's idea [21] the POD modes are expressed as linear combinations of the snapshots :

$$\boldsymbol{\Phi}^k(\boldsymbol{x}) = \sum_{i=1}^{N_t} b^k_i\boldsymbol{u}^i(\boldsymbol{x}) \text{ for } k = 1..N_r$$

The vectors $[b^r_i]_{i=1\cdots N_t}$ are found to be the eigenvectors of the $N_t \times N_t$ correlation matrix R, $R_{ij} = (\boldsymbol{u}^i,\boldsymbol{u}^j)$, corresponding to the N_r highest eigenvalues, while the $\hat{a}^i_k$ are equal to the scalar products $(\boldsymbol{u}^i,\boldsymbol{\Phi}^r)$.
In the case of forced flow, the snapshots depend on the control law $c(t)$ used. In this work we consider POD basis derived from numerical simulations obtained using several different control laws. Indeed, there are a number of other parameters that could be varied, but since our aim is to study the effect of a control law, we set ourselves in the following framework :

- Time instants, Reynolds number, domain geometry, placement of the actuators will be the same for all the snapshots in the database.
- The control law $c(t)$ will be varied

The data set used for the POD is therefore written :

$$\{\boldsymbol{u}^{i,\ell}(\boldsymbol{x}) =\}_{i=1..N_t,\ell=1..N_c}$$

where N_c denotes the number of control laws considered. If $\mathcal{C} = \{c_1, c_2,\cdots,c_{N_c}\}$ is the set of control laws used to obtain the database, the ensuing POD basis is denoted $\boldsymbol{\Phi}(\mathcal{C})$. In the first part of this work, $\mathcal{C}$ is reduced to a single element which we denote $c(t)$.

2.2.2 Dealing with the boundary conditions

In the non-controlled case, we lift the boundary conditions on the velocity fields by defining a new set of snapshots :

$$\boldsymbol{w}^i(\boldsymbol{x}) = \boldsymbol{u}^i(\boldsymbol{x}) - \bar{\boldsymbol{u}}(\boldsymbol{x})$$

where $\bar{\boldsymbol{u}}$ is some reference velocity field that satisfies the same boundary conditions as the snapshots. In the present configuration, it can be the steady unstable solution, or a time average of the snapshots $\boldsymbol{u}^k$.
When an extra boundary condition is imposed on the cylinder for control purposes, the snapshots are chosen to be :

$$\boldsymbol{w}^i(\boldsymbol{x}) = \boldsymbol{u}^i(\boldsymbol{x}) - \bar{\boldsymbol{u}}(\boldsymbol{x}) - c(t^i)\boldsymbol{u}_c(\boldsymbol{x})$$

where $\boldsymbol{u}_c(\boldsymbol{x})$ satisfies the following criteria :

$$\boldsymbol{u}_c(\boldsymbol{x}) = \bar{\boldsymbol{u}}(\boldsymbol{x}) \text{ on } \Gamma\backslash\Gamma_c, \boldsymbol{u}_c(\boldsymbol{x}) = 1 \text{ on } \Gamma_c$$

In practice we use the velocity field proposed in [8] :

$$\boldsymbol{u}_c(\boldsymbol{x}) = \frac{1}{c^\star}(\bar{\boldsymbol{u}}'(\boldsymbol{x}) - \bar{\boldsymbol{u}}(\boldsymbol{x}))$$

where $\bar{\boldsymbol{u}}'$ is obtained in the same way as $\bar{\boldsymbol{u}}$ but applying a constant control equal to $c^\star$ on Γ_c . The low-dimensional solution is now written :

$$\boldsymbol{u}_R(\boldsymbol{x}, t) = \bar{\boldsymbol{u}}(\boldsymbol{x}) + c(t)\boldsymbol{u}_c(\boldsymbol{x}) + \sum_{k=1}^{N_r} a_k(t)\boldsymbol{\Phi}^k(\boldsymbol{x}) \tag{2}$$

2.3 POD-Galerkin Reduced Order Model

Galerkin projection of the incompressible Navier-Stokes equations onto the first N_r POD modes yields a system of ordinary differential equations :

$$\begin{cases} \dot{a}_r(t) &= \boldsymbol{A}^{\boldsymbol{G}}_r + \boldsymbol{C}^{\boldsymbol{G}}_{kr} a_k(t) + \boldsymbol{B}^{\boldsymbol{G}}_{ksr} a_k(t) a_s(t) + \mathcal{P}_r \\ & + \quad \boldsymbol{E}^{\boldsymbol{G}}_r \dot{c}(t) + \boldsymbol{F}^{\boldsymbol{G}}_r c^2(t) + \boldsymbol{G}^{\boldsymbol{G}}_r c(t) + \boldsymbol{H}^{\boldsymbol{G}}_{kr} a_k(t) c(t) \\ a_r(0) &= a_r^0 \\ 1 \leq r \leq N_r & \end{cases} \tag{3}$$

where :

$$
\begin{aligned}
&\boldsymbol{A}_r^{\boldsymbol{G}} = -((\overline{u}\cdot\nabla)\overline{u}, \boldsymbol{\Phi}^r) + \frac{1}{Re}(\Delta\overline{u}, \boldsymbol{\Phi}^r)\\
&\boldsymbol{B}_{ksr}^{\boldsymbol{G}} = -((\boldsymbol{\Phi}^k\cdot\nabla)\boldsymbol{\Phi}^s, \boldsymbol{\Phi}^r)\\
&\boldsymbol{C}_{kr}^{\boldsymbol{G}} = -((\overline{u}\cdot\nabla)\boldsymbol{\Phi}^k, \boldsymbol{\Phi}^r) - ((\boldsymbol{\Phi}^k\cdot\nabla)\overline{u}, \boldsymbol{\Phi}^r) + \frac{1}{Re}(\Delta\boldsymbol{\Phi}^k, \boldsymbol{\Phi}^r)\\
&\boldsymbol{E}_r^{\boldsymbol{G}} = (u_c, \boldsymbol{\Phi}^r)\\
&\boldsymbol{G}_r^{\boldsymbol{G}} = -((\overline{u}\cdot\nabla)u_c, \boldsymbol{\Phi}^r) - ((u_c\cdot\nabla)\overline{u}, \boldsymbol{\Phi}^r) + \frac{1}{Re}(\Delta u_c, \boldsymbol{\Phi}^r)\\
&\boldsymbol{F}_r^{\boldsymbol{G}} = ((u_c\cdot\nabla)u_c, \boldsymbol{\Phi}^r)\\
&\boldsymbol{H}_{rk}^{\boldsymbol{G}} = ((u_c\cdot\nabla)\boldsymbol{\Phi}^k, \boldsymbol{\Phi}^r) + ((\boldsymbol{\Phi}^k\cdot\nabla)u_c, \boldsymbol{\Phi}^r)\\
&\mathcal{P}_r = (\nabla p, \boldsymbol{\Phi}^r)
\end{aligned}
$$

We note that since the snapshots satisfy the continuity equation, the modes do also. This implies that the pressure term $\mathcal{P}_r$ is equal to $\int_{\partial\Omega} p\boldsymbol{\Phi}^r\, ds$. If velocity field is constant at the boundaries, the POD modes are zero there. The pressure term therefore disappears completely.
Setting :

$$
\boldsymbol{X}_r^{\boldsymbol{G}} \quad = \quad \Big[\boldsymbol{A}_r^{\boldsymbol{G}},\, \{\boldsymbol{B}_{ksr}^{\boldsymbol{G}}\}_{k,s=1\cdots N_r},\, \{\boldsymbol{C}_{kr}^{\boldsymbol{G}}\}_{k=1\cdots N_r},\, \boldsymbol{E}_r^{\boldsymbol{G}},\, \boldsymbol{F}_r^{\boldsymbol{G}},\, \boldsymbol{G}_r^{\boldsymbol{G}},\, \{\boldsymbol{H}_{kr}^{\boldsymbol{G}}\}_{k=1\cdots N_r}\Big]^t
$$

and

$$
\begin{aligned}
\boldsymbol{f}(\boldsymbol{a}(t), c(t), \dot{c}(t)) \quad = \quad & \Big[1,\, \{a_k(t)a_s(t)\}_{k,s=1\cdots N_r},\, \{a_k(t)\}_{k=1\cdots N_r},\\
& \dot{c}(t),\, c^2(t),\, c(t),\, \{a_k(t)c(t)\}_{k=1\cdots N_r}\Big]
\end{aligned}
$$

the first equation in (3) can be written in the compact form :

$$
\dot{a}_r(t) = \boldsymbol{f}(\boldsymbol{a}(t), c(t), \dot{c}(t)) \cdot \boldsymbol{X}_r^{\boldsymbol{G}}
$$

The initial value problem (3) is a reduced order model of the Navier-Stokes equations, called the POD-Galerkin model. Such a model might be inaccurate for it may not take into account enough of the dynamics. Indeed, although a number N_r of modes can be sufficient to capture most of the flow energy, the neglected modes continue to play an important role in the flow dynamics through their interaction with the conserved ones. The difference between the solutions $a_r(t)$ of (3), and the coefficients $\hat{a}_r(t)$ obtained by projecting the numerical data onto the POD modes ($\hat{a}_r(t^i) = \hat{a}_r^i$), has been underlined in several papers [8, 2, 7]. It is therefore interesting to build a model that exploits the knowledge one has of the dynamics, that is the set of temporal projection coefficients $\hat{a}_r^i$. This is the subject of the next section.

3 Robust low order models

3.1 Calibration method

The idea of calibration is to keep the structure of the above model while adjusting the coefficients of the system so its solution is closer to the desired one. In previous work [9, 8], it was shown that robust low order models could be obtained by solving the minimization problem :

$$\begin{aligned} &\min_{a,\boldsymbol{X}} \sum_{r=1}^{N_r} \int_0^T \left(a_r(t) - \hat{a}_r(t)\right)^2 dt \\ &\text{subject to} \qquad \dot{a}_r(t) = \boldsymbol{f}(\boldsymbol{a}(t), c(t), \dot{c}(t)) \cdot \boldsymbol{X}_r \end{aligned} \tag{4}$$

This *state calibration* method, which involves solving a strongly non-linear system, works well as long as the number of snapshots considered remains limited. For a large number of snapshots, the computational costs are excessive.
Another method was suggested in [9], and has been experimented, for a case with no control, in [4, 3, 7] with good results. It consists in choosing $\boldsymbol{X}$ as the solution of :

$$\min_{\boldsymbol{X}} \sum_{r=1}^{N_r} \int_0^T \left(\dot{\hat{a}}_r(t) - \boldsymbol{f}(\hat{\boldsymbol{a}}(t), c(t), \dot{c}(t)) \cdot \boldsymbol{X}_r\right)^2 dt \tag{5}$$

This method can be interpreted as approximating the error

$$e_r(t) = \dot{\hat{a}}_r(t) - \boldsymbol{f}(\hat{\boldsymbol{a}}(t), c(t), \dot{c}(t)) \cdot \boldsymbol{X}_r^{\boldsymbol{G}}$$

by a quadratic function of all the non-discarded temporal coefficients, $c(t)$ and $\dot{c}(t)$.
Other choices for the approximation of e_r lead to partial calibration problems.
For example, if we suppose $e_r \approx \boldsymbol{A}_r^{\boldsymbol{E}} + \boldsymbol{C}_{kr}^{\boldsymbol{E}} a_k + \boldsymbol{G}^{\boldsymbol{E}} c$ then we will solve :

$$\min_{\boldsymbol{X}_1^{\boldsymbol{C}}} \sum_{r=1}^{N_r} \int_0^T \left(\dot{\hat{a}}_r(t) - \boldsymbol{f}_1(t) \cdot \boldsymbol{X}_{r,1}^{\boldsymbol{C}} - \boldsymbol{f}_2(t) \cdot \boldsymbol{X}_{r,2}^{\boldsymbol{G}}\right)^2 dt \tag{6}$$

where

$$\begin{aligned} \boldsymbol{X}_{r,1}^{\boldsymbol{C}} &= \left[\boldsymbol{A}_r^{\boldsymbol{C}},\, \{\boldsymbol{C}_{kr}^{\boldsymbol{C}}\}_{k=1\cdots N_r},\, \boldsymbol{G}_r^{\boldsymbol{C}}\right]^t \\ \boldsymbol{X}_{r,2}^{\boldsymbol{G}} &= \left[\{\boldsymbol{B}_{ksr}^{\boldsymbol{G}}\}_{k,s=1\cdots N_r},\, \boldsymbol{E}_r^{\boldsymbol{G}},\, \boldsymbol{F}_r^{\boldsymbol{G}},\, \{\boldsymbol{H}_{kr}^{\boldsymbol{G}}\}_{k=1\cdots N_r}\right]^t \end{aligned}$$

and

$$\begin{aligned} \boldsymbol{f}^1(t) &= \left[1,\, \{a_k(t)\}_{k=1\cdots N_r},\, c(t)\right] \\ \boldsymbol{f}^2(t) &= \left[\{a_k(t)a_s(t)\}_{k,s=1\cdots N_r},\, \dot{c}(t),\, c(t),\, \{a_k(t)c(t)\}_{k=1\cdots N_r}\right] \end{aligned}$$

Of course, other choices of which terms to calibrate or not can be made. For a general formulation we denote N_{cal} the number of terms of vector $\boldsymbol{X}_r$ that are calibrated, and we have $N_{cal} \leqslant N_r^2 + 2 \times N_r + 4$. Whatever the choice for N_{cal}, this approach is always much more efficient than (4) since it involves solving N_r linear symmetric systems of size N_{cal}^2 :

$$\int_0^T \boldsymbol{f}_1^t(t)\boldsymbol{f}_1(t)\, dt \quad \boldsymbol{X}_{r,1}^{\boldsymbol{C}} = \int_0^T \boldsymbol{f}_1^t(t) \left(\dot{\hat{a}}_r(t) - \boldsymbol{f}_2(t) \cdot \boldsymbol{X}_{r,2}^{\boldsymbol{G}}\right) dt \tag{7}$$

The more terms of $\boldsymbol{X}_r$ are calibrated, the more the problem becomes ill-conditioned. For this reason we choose not to calibrate the N_r^3 terms $\boldsymbol{B}_{ksr}$.

Once the model has been calibrated to fit a particular control law $c(t)$, it can of course be integrated using another control law. Denoting the input control law $c^{\mathrm{I}}(t)$, the calibrated model is written :

$$\mathcal{R}(\{c\}) \begin{cases} \dot{a}_r(t) &= \boldsymbol{f}(\hat{\boldsymbol{a}}(t), c^{\mathrm{I}}(t), \dot{c}^{\mathrm{I}}(t)) \cdot \boldsymbol{X}_r \\ a_r(0) &= a_r^0 \\ 1 \leq r \leq N_r \end{cases} \tag{8}$$

where by denoting $\mathcal{R}(\{c\})$ the model we put in evidence that it was calibrated using the control $c(t)$.

3.2 Well-posedness and robustness

3.2.1 Calibration with feedback control laws

We suppose that the control is obtained using a proportional feedback law (Sec.2.1) :

$$c(t) = \sum_{j=1}^{N_s} \mathsf{K}_j v(\boldsymbol{x}_j, t)$$

We can now consider two different calibration problems. The first is the problem (5), the second is :

$$\min_{\boldsymbol{X}} \sum_{r=1}^{N_r} \int_0^T \left(\dot{\hat{a}}_r(t) - \boldsymbol{f}(\hat{\boldsymbol{a}}(t), \hat{c}(t), \dot{\hat{c}}(t)) \cdot \boldsymbol{X}_r \right)^2 dt \tag{9}$$

where $\hat{c}$ is defined by :

$$\hat{c}(t) = \mathsf{K}_j v_R(\boldsymbol{x}_j, t) = \mathsf{K}_j \left(\bar{\boldsymbol{v}}(\boldsymbol{x}_j) + \hat{c}(t) \boldsymbol{v}_c(\boldsymbol{x}_j) + \sum_{r=1}^{N_r} \hat{a}_r(t) \boldsymbol{\Phi}_v^r(\boldsymbol{x}_j) \right) \tag{10}$$

This last approach makes the reduced order model a feedback model, which is useful if we want to use the model to determine an optimal feedback law. The problem is however under-determined.
We reformulate (10) to clearly show the dependency of $\hat{c}$ on $\hat{\boldsymbol{a}}$:

$$\hat{c}(t) = \kappa_0 + \sum_{r=1}^{N_r} \kappa_r \hat{a}_r(t) \tag{11}$$

where

$$\kappa_0 = \frac{\mathsf{K}_j}{1 - \mathsf{K}_i \boldsymbol{v}_c(\boldsymbol{x}_i)} \quad \bar{\boldsymbol{v}}(\boldsymbol{x}_j) \quad , \quad \kappa_r = \frac{\mathsf{K}_j}{1 - \mathsf{K}_i \boldsymbol{v}_c(\boldsymbol{x}_i)} \quad \boldsymbol{\Phi}_v^r(\boldsymbol{x}_j)$$

We now look at the partial-calibration problem described above. The function $\boldsymbol{f}^1$ that appears in system (7) can be reformulated :

$$\boldsymbol{f}^1(t) = \left[1,\ \{\hat{\boldsymbol{a}}_k(t)\}_{k=1\cdots N_r},\ \kappa_0 + \kappa_\ell \hat{\boldsymbol{a}}_\ell(t)\right]$$

System (7) is therefore rank deficient. The problem remains if more of the system coefficients are calibrated, and according to the choice made the rank of the problem matrix can even diminish with respect to N_{cal}.
This difficulty can however be solved by using one of the two methods proposed in the section (3.3). Finally, the proportional feedback reduced order model is written :

$$\mathcal{R}^{\mathrm{F}}(\{\hat{c}\}) \begin{cases} \dot{a}_r(t) &= \boldsymbol{f}(\boldsymbol{a}(t), c^{\mathrm{F}}(t), \dot{c}^{\mathrm{F}}(t)) \cdot \boldsymbol{X}_r \\ c^{\mathrm{F}}(t) &= \displaystyle\sum_{j=1}^{N_s} \mathsf{K}_j \left(\bar{\boldsymbol{v}}(\boldsymbol{x}_j) + c^{\mathrm{F}}(t)\boldsymbol{v}_c(\boldsymbol{x}_j) + \sum_{r=1}^{N_r} a_r(t)\boldsymbol{\Phi}_v^r(\boldsymbol{x}_j) \right) \\ a_r(0) &= a_r^0, \quad c^{\mathrm{F}}(0) = \hat{c}(0) \\ 1 \leq r \leq N_r \end{cases} \tag{12}$$

3.2.2 Instability issues

The system solved for calibration can be ill-posed even in cases different to the one just described. To understand why this is, it is sufficient to go back to the *state calibration method* mentioned at the beginning of the section. Solving the minimization problem (4) involves solving a non-linear system for which the uniqueness of solution is not guaranteed. The state calibration functional can therefore have several local optima, and so there are several possible choices for $\boldsymbol{X}$ that will lead to a low value of the error $\|\hat{\boldsymbol{a}} - \boldsymbol{a}\|$. Since these choices should also be good choices for the minimization problem (6), the matrix $\int_0^T \boldsymbol{f}_1^t \boldsymbol{f}_1 \, dt$ in (7) is in general almost singular. A model obtained by inverting this matrix is most often very unstable. To overcome this problem we propose a Tikhonov type regularization method which we describe in the next section.

3.2.3 Robustness

While a calibrated reduced order model $\mathcal{R}(\{c\})$ works well when integrated with $c^{\mathrm{I}}(t) = c(t)$, its behavior when integrated with a different control law is unpredictable. As such, the reduced order model can difficultly be used for estimation and optimization purposes.
In the literature several methods are proposed for adapting reduced order modeling for control purposes, some successful examples can be found in [13, 19, 1]. However for those cases, no calibration seems necessary for the models to work, but this is not the case for general control problems as shown in the following.
The originality of the model we propose hereafter, is the combination of multi control data sets with the calibration procedure. Such a model is fast to build and yet remains accurate for different control inputs.

3.3 Building a robust low order model

In this section we describe a method to make the reduced order model stable and robust.

3.3.1 Tikhonov regularization

Correctly solving (4) can be done by applying a quasi-Newton method, initialized with $\hat{\boldsymbol{a}}$ and $\boldsymbol{X}_1^{\boldsymbol{G}}$. It therefore seems reasonable to solve the following regularized problem, instead of (6) :

$$\begin{aligned}\min_{\boldsymbol{X}_1^{\boldsymbol{C}}} \sum_{r=1}^{N_r} \int_0^T \left(\dot{\hat{a}}_r(t) - \boldsymbol{f}_1(\hat{\boldsymbol{a}}(t)) \cdot \boldsymbol{X}_{r,1}^{\boldsymbol{C}} \right. & - \left. \boldsymbol{f}_2(\hat{\boldsymbol{a}}(t)) \cdot \boldsymbol{X}_{r,2}^{\boldsymbol{G}}\right)^2 dt \\ & + \alpha \textstyle\sum_{r=1}^{N_r} \|\boldsymbol{X}_{r,1}^{\boldsymbol{C}} - \boldsymbol{X}_{r,1}^{\boldsymbol{G}}\|^2\end{aligned} \tag{13}$$

where α is the regularization parameter.
The parameter α can be chosen by a classical technique. We start by plotting, for a set of values of α in $[10^{-6}, 10^{-2}]$, the error $\sum_r \|\dot{a}_r - \dot{\hat{a}}_r\|^2$ versus the coefficient variation $\|\boldsymbol{X}_1^{\boldsymbol{C}} - \boldsymbol{X}_1^{\boldsymbol{G}}\|^2$. This leads to a classical Tikhonov L-shaped curve of which the corner point is optimal in the sense that it is a good compromise between the error on the dynamics and the distance from the original coefficients [12]. The value of α corresponding to this point can be chosen to perform the calibration procedure.

3.3.2 Calibrating over more than one control law

In this paragraph we look at the changes to be made to the reduced order model when the data set includes simulations obtained using different control laws. Letting :

$$\hat{a}_r^{i,\ell} = \left(\boldsymbol{u}^{i,\ell}, \boldsymbol{\Phi}^r\right)$$

the calibration problem becomes :

$$\min_{\boldsymbol{X}} \sum_{r=1}^{N_r} \sum_{\ell=1}^{N_c} \int_0^T \left(\dot{\hat{a}}_r^\ell(t) - \boldsymbol{f}(\hat{\boldsymbol{a}}^\ell(t), c^\ell(t), \dot{c}^\ell(t)) \cdot \boldsymbol{X}_r\right)^2 dt \tag{14}$$

We remark that although the size of the snapshots database is proportional to the number of controls considered, the size of the calibration problem remains constant. Furthermore, if $N_c > 1$ the rank deficiency discussed for proportional feedback no longer occurs.
The main idea is that as the number of controls N_c is increased, although the model can become a little less precise for the reference control, it is much more accurate for other control laws. In the next section we show some successful examples of this method at different Reynolds number, and for different kinds of control laws.
We refer to a model built using N_c control laws as an N_c-control model. Such a model is denoted $\mathcal{R}_{\mathcal{C}}$ where $\mathcal{C} = \{c_1, \cdots, c_{N_c}\}$.

4 Results and discussion

The described technique was applied in order to build a low order model of the actuated flow around the confined square cylinder in various configurations. We tested the prediction capabilities of the model for two different Reynolds number, $Re = 60$ and $Re = 150$, with precomputed and feedback control laws. In particular we built different models with one and more control laws and we analyzed their predictions with different controls.

In all the examples presented in the following, actuation is started only once the flow is fully developed. With the control turned on the simulation is performed for about seven vortex shedding cycles, and $N_t \approx 200$ snapshots are saved. $T \simeq 50$ is the non-dimensional duration of the time interval. The number of POD modes retained for the reduced order model is $N_r = 40$ for the case $Re = 60$ and $N_r = 60$ for the case $Re = 150$.

We measure the accuracy of the model $\mathcal{R}(\mathcal{C})$ in the following way :

– Time coefficients dynamics :
  For a given value of r, plot $a_r(t)$, solution of $\mathcal{R}(\mathcal{C})$ with input $c^{\mathrm{I}}(t)$, against $\hat{a}_r(t)$, projection of the full order solution onto the POD basis $\boldsymbol{\Phi}(\mathcal{C})$. In the examples $r = 3$ is usually chosen because it was the mode for which the differences between models were the most remarkable.

– Computation of the integration error :

$$\mathcal{E}(\mathcal{C}, c^{\mathrm{I}}) = \|\boldsymbol{a} - \hat{\boldsymbol{a}}\| / \|\hat{\boldsymbol{a}}\|$$

  where $\|\boldsymbol{a}\| = \displaystyle\int_0^T \sum_r a_r^2(t)\, dt$

In the examples with feedback laws we use only one sensor placed in the cylinder wake. Choosing the center of the cylinder as the origin of a coordinate system, we denote $\boldsymbol{x}_s = (x_s, y_s)$ the position of the sensor. The integration error $\mathcal{E}^{\mathrm{F}}(\mathcal{C}, \mathsf{K}^{\mathrm{I}})$ is measured in the same way as for the non-feedback case.

Our first goal is that the model should be able to reproduce the DNS data to which is was fitted, we therefore expect $\mathcal{E}(\mathcal{C}, c^{\mathrm{I}})$ to be small if $c^{\mathrm{I}} \in \mathcal{C}$. Our second goal is that the model be robust to parameter variation. As the difference between $c^{\mathrm{I}}(t)$ and the controls in $\mathcal{C}$ increases, the error $\mathcal{E}(\mathcal{C}, c^{\mathrm{I}})$ grows. We seek a model for which this growth rate is as low as possible.

4.1 Divergence of a classical Reduced Order Model

A simulation at $Re = 60$ was performed using feedback control with a sensor placed at $(x_s, y_s) = (0.7, 0.0)$ and $\mathsf{K} = 1$. We denote $c(t)$ the control law obtained at the end of simulation.

We compare the results obtained with the POD Galerkin model (3) and with the calibrated model $\mathcal{R}(\{c\})$ (see system (8) for model formulation). The model integration error $\mathcal{E}(\{c\}, c)$ is equal to 23% for the non-calibrated model, and to 0.136% for the calibrated model.

For a feedback model, the difference is even more important. We integrated the feedback system (12) with $\mathsf{K} = 1$, once with $\boldsymbol{X}$ obtained by Galerkin projection, and once

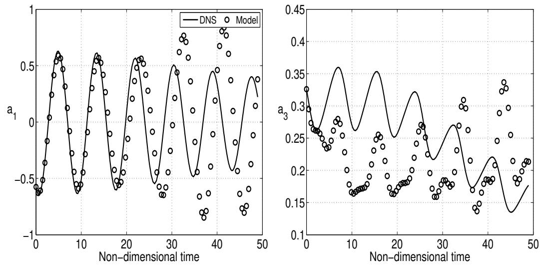

FIG. 3 – Projection of the DNS simulations onto POD modes vs. integration of the dynamical system (12) with $\boldsymbol{X} = \boldsymbol{X}^G$

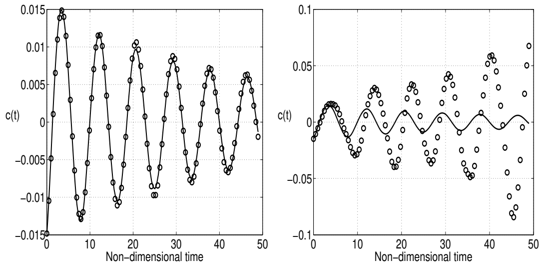

FIG. 4 – c_1 (continuous line) versus c^{F}, when the model is calibrated (left) and when it is not (right)

with $\boldsymbol{X}$ calibrated as described in 3.2.1. We obtained an integration error $\mathcal{E}^{\mathrm{F}}(\{\hat{c}\}, 1)$ of 117% in the first case, against an error of 4% in the other. An example of the errors in terms of time dynamics that the non-calibrated model can produce are shown in Fig.3. In Fig.4 we plot the control law $c^{\mathrm{F}}(t)$ computed when integrating the feedback model, and on the same figure, the original control law $c(t)$. Results for the non-calibrated case are plotted on the right : the distance between $c^{\mathrm{F}}(t)$ and $c(t)$ increases with time, meaning that at each time step, new errors are added to the model. Calibration is therefore all the more essential when considering feedback control.

In order to calibrate, regularization is needed to get well-conditioned inverse problems as shown in the following. However, the choice of the parameter α is not an easy one. For example, we performed a simulation at $Re = 150$ using a feedback control with a sensor placed at $(x_s, y_s) = (0.7, 0.0)$ and $\mathsf{K} = 0.8$. The calibration described in 3.3.1 was performed with $\alpha \approx 0$. This led to an ill-conditioned system to solve and to a model that was not very accurate, and not robust at all to parameter variations. The effect of α on model results is shown in Fig.5. The two top figures show the third modal coefficient obtained by projection and by integrating the model with $\mathsf{K} = 0.8$. On the left, we plot the results obtained when the model was built with $\alpha = 1.6 * 10^{-6}$: at the end of the time period the model diverges from the DNS results. With a higher value, $\alpha = 10^{-3}$, this problem no longer occurs, as shown on the right. The same test was then performed with a different value of K in order to see the models capacity to

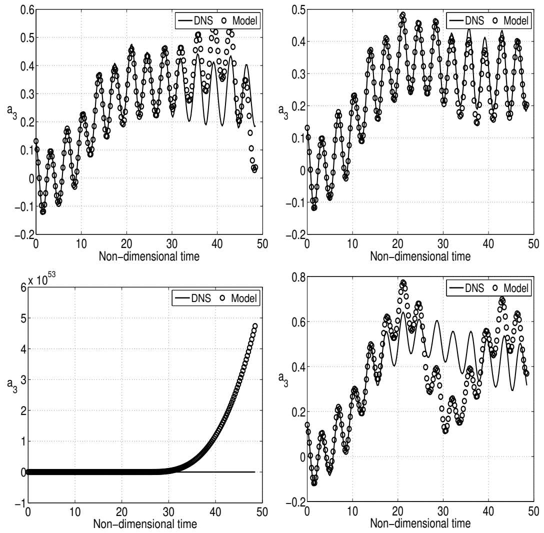

FIG. 5 – a_3 DNS (continuous line) with $\mathsf{K} = 0.8$ (top) and $\mathsf{K} = 1.3$ (bottom) versus a_3 obtained when the model is calibrated with $\alpha = 1.6 * 10^{-6}$ (left) and when $\alpha = 10^{-3}$ (right)

predict dynamics to which it was not fitted. The results are shown in the same figure : divergence was immediate for a low value of α, whereas for a higher value, the model, although not accurate, was at least stable. It appears that, when using an higher regularization parameter, the calibration system is well conditioned, the model more accurate and more stable when integrated with a different control law to those used for calibration. In the following the parameter α is determined using the L-method with the restriction that any values of α below a certain threshold are excluded.

4.2 Testing model robustness

In this section we present the improvements brought to model robustness by introducing calibration over several control laws. For both Reynolds numbers, $Re = 60$ and $Re = 150$, the same experiment was performed :

Step 1 : Build 1- , 2- and 3-control models

We started by choosing three control laws which we denote $c_1(t)$, $c_2(t)$ and $c_3(t)$. For each control we performed a simulation of the Navier-Stokes equations, saving 200 snapshots for each simulation. We then defined seven control sets :

$$\text{Three 1-control sets : } \mathcal{C}^1 = \{c_1\}, \mathcal{C}^2 = \{c_2\}, \mathcal{C}^3 = \{c_3\}$$

$$\text{Three 2-control sets : } \mathcal{C}^4 = \{c_1, c_2\}, \mathcal{C}^5 = \{c_1, c_3\}, \mathcal{C}^6 = \{c_2, c_3\}$$

$$\text{One 1-control set : } \mathcal{C}^7 = \{c_1, c_2, c_3\}$$

For each control set $\mathcal{C}^i$, we computed a POD basis $\mathbf{\Phi}(\mathcal{C}^i)$ as described in section 2.2.1 and a calibrated reduced order model $\mathcal{R}(\mathcal{C}^i)$ by solving problem (14).
In the following we refer to $c_1(t)$, $c_2(t)$ and $c_3(t)$ as the *model control laws*.

Step 2 : Run the model with different control laws

We next chose several other control laws which we denote $c_j^{test}(t)$. Each of these *test control laws* was used as input for the Navier-Stokes equations, and for the seven reduced order models $\mathcal{R}(\mathcal{C}^i)$ described above. The snapshots from the Navier-Stokes simulations were projected onto the seven POD bases $\mathbf{\Phi}(\mathcal{C}^i)$. This procedure made it possible to compute the model integration errors $\mathcal{E}_i^j = \mathcal{E}(\mathcal{C}^i, c_j^{test})$, and compare the efficiency of each model.
For measuring model robustness, it is useful to have some idea of how much the dynamics we are trying to predict, differ from those included in the model. We therefore need to find a way, for each model, to measure the distance between the $N_t \times N_c$ snapshots that were used to build it, and the N_t snapshots obtained using a *test* control law. To do this we proceed in the following way : if the control set $\mathcal{C}^i$ is composed of N_c control laws, then the *distance* between the simulations associated to $\mathcal{C}^i$, and the one obtained using $c_j^{test}(t)$, is defined as :

$$\Delta_i^j = \frac{1}{N_c} \sum_{l=1}^{N_c} \left(\|\hat{\boldsymbol{a}}^l - \hat{\boldsymbol{a}}^j\| / \|\hat{\boldsymbol{a}}^l\| \right)$$

where the terms $\hat{\boldsymbol{a}}^n$ ($n = j$ or $n = 1 \cdots l$) result from projecting the snapshots onto the POD basis $\mathbf{\Phi}(\mathcal{C}^i)$.
The results are plotted for in Fig. 8 and Fig. 12. For each value of model i, the model integration error $\mathcal{E}_i^j$ is plotted versus the *distance* Δ_i^j. We note that the three controls used to build the models were in fact included in the test set, which explains why there are 3 points at $\Delta_i^j = 0$.

4.3 Results for $Re = 60$

In Fig.6 we plot the control laws used to build the models. For each control law we plot the third modal coefficient $\hat{a}_3(t)$ to give an idea of the dynamics induced. The figure also shows the prediction for this coefficient given by the 3-control model $\mathcal{R}(\mathcal{C}^7)$. The model results are accurate : the reduced order model was successfully calibrated to fit several dynamics.

Eleven extra control laws were used for testing. A few examples are plotted in Fig. 7. For these examples we also plot the third modal coefficient obtained by projection and by model integration. Some discrepancies in coefficient amplitude are observed, but overall the model predicts the right time dynamics.
In Fig. 8 we look at the results obtained with the different models, using the distances and errors described above. The first point to be made is that the model error is almost zero when the distance from the model is zero. This confirms that 1-control models work well when integrated with the control law to which they were fitted. The errors

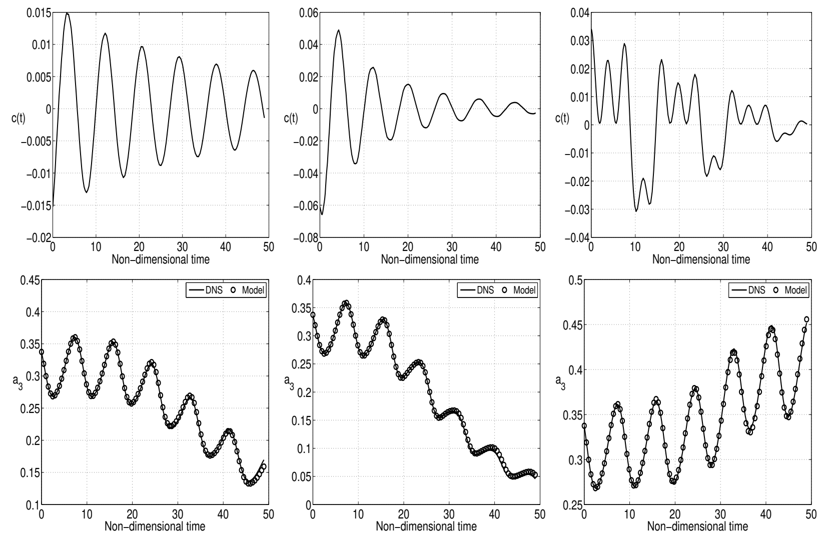

FIG. 6 – Control laws used to build the models (top) ; a_3 DNS (continuous line) vs prediction by 3-control model (symbols)

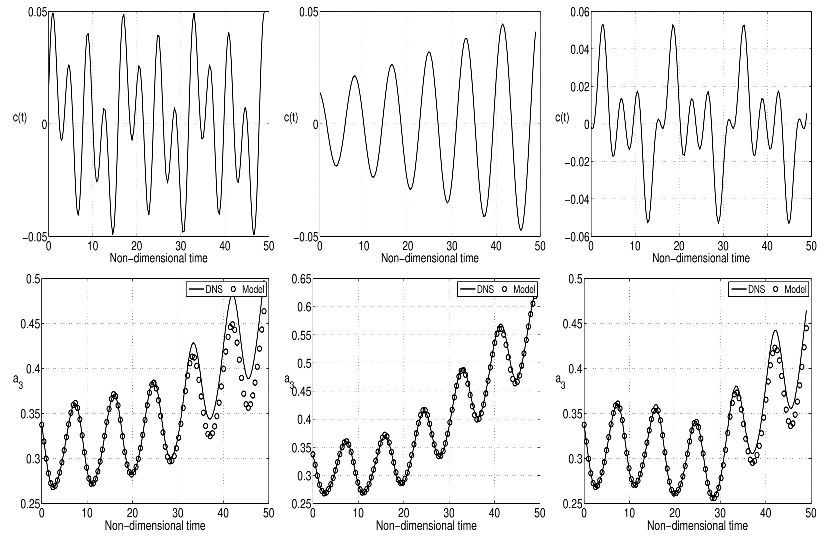

FIG. 7 – Control laws and time coefficients used for testing the model

then increase with the distance from the model, as was expected.
The graph highlights the disadvantage of 1-control models. In the best case the difference between projection and prediction coefficients becomes higher than 20% as soon as the distance from the model exceeds 40%. In contrast, for the 2-control and 3-control

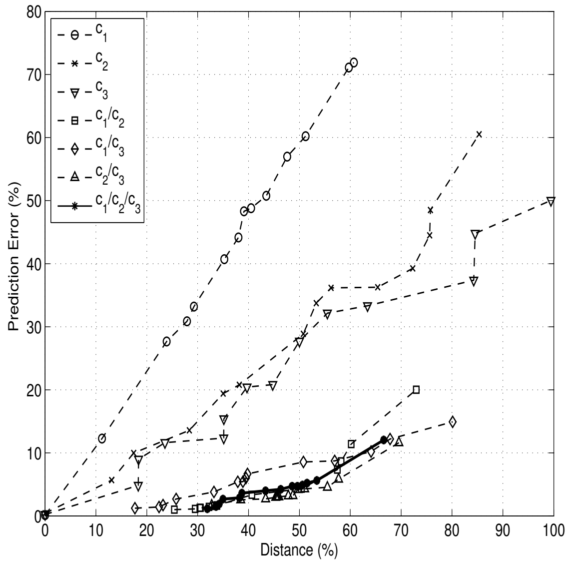

FIG. 8 – Prediction errors obtained using 1-control, 2-control and 3-control models

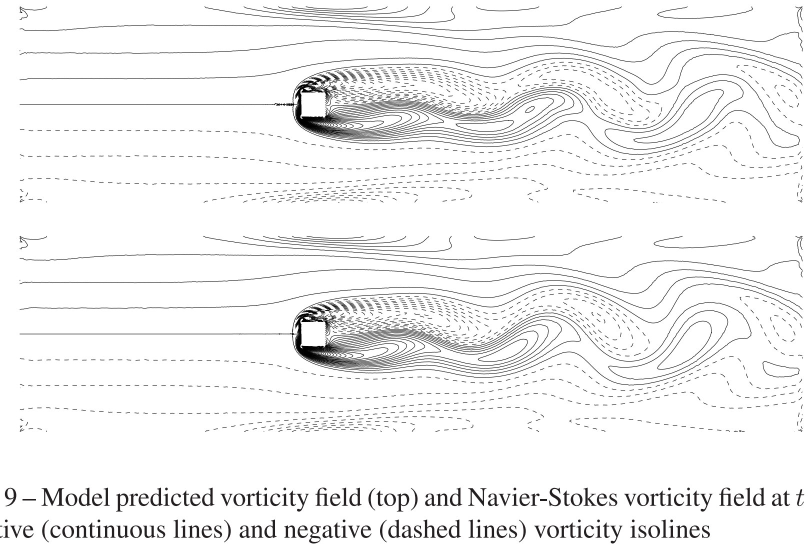

FIG. 9 – Model predicted vorticity field (top) and Navier-Stokes vorticity field at $t = T$. Positive (continuous lines) and negative (dashed lines) vorticity isolines

models, the error stays under 20%, even when the distance increases. In Fig. 9 we plot isolines of the vorticity at time $t = T$ for one of the test control laws (the third control law in Fig.7). Time coefficients were obtained by solving $\mathcal{R}(\mathcal{C})$ with $\mathcal{C} = \{c_1, c_2\}$. The velocity field was then reconstructed using the first ten of these coefficients and the first ten POD modes in $\Phi(\mathcal{C})$. The reconstructed vorticity is presented along with the vorticity obtained by running the Navier-Stokes equations with the test control law.

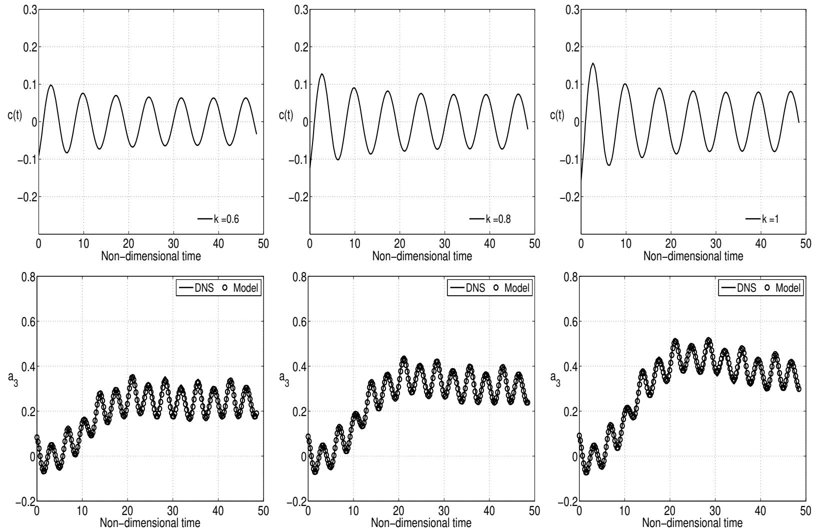

FIG. 10 – Control laws used to build the models (top) ; a_3 DNS (continuous line) vs prediction by 3-control model (symbols)

The controls used to build the model caused a slight decrease in vortex size (see Fig. 6, bottom left) whereas actuation used in the test caused a slight increase in vortex size (see Fig. 7, bottom right) . We note that the model was able to predict such features, and that at the end of the simulation time, the structure of reconstructed flow is almost identical to that of the real flow. In contrast, the 1-controls weren't able to identify this. If the same reconstruction is performed using $\mathcal{C} = \{c_1\}$ for example, the flow appears almost stable at $t = T$, meaning the model predicted the opposite behavior to what actually happened.

4.4 Results for $Re = 150$

For $Re = 150$ only feedback control laws are used both to build the models and to perform the tests. In Fig.10 the three feedback control laws used to calibrate the model are shown. The laws are obtained with sensors placed at $(x_s, y_s) = (0.7, 0.0)$ and by using gains $\mathsf{K} = 0.6$, $\mathsf{K} = 0.8$ and $\mathsf{K} = 1$. The figure also shows the third modal coefficients given by integrating the 3-control feedback model with each gain. Although the control laws induce different dynamics, the model is able to give an accurate prediction in all three cases. Six extra control laws were used for testing, each corresponding to a different choice of K. A few examples, with corresponding coefficients $\hat{a}_3(t)$ are plotted in Fig.11. It appears that the dynamics are quite different when the distance, between the gain value and gains included in the model, is large. For example, when using a gain $\mathsf{K} = 0.1$ the average value of $\hat{a}_3(t)$ is low compared to that obtained with $\mathsf{K} = 1$. However, the 3-control model again gives an overall good prediction of the time dynamics. Fig.12 is built the same way as Fig. 8. In particular the graph

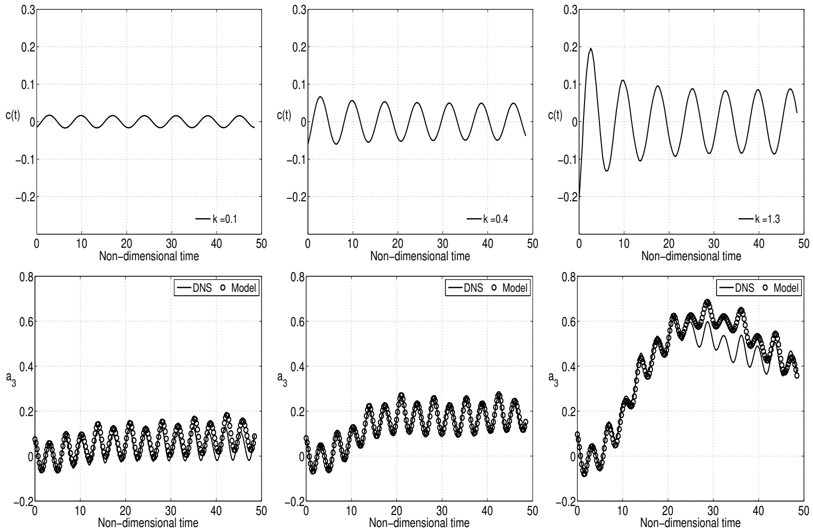

FIG. 11 – Control laws used to test the models (top) ; a_3 DNS (continuous line) vs prediction by 3-control model (symbols)

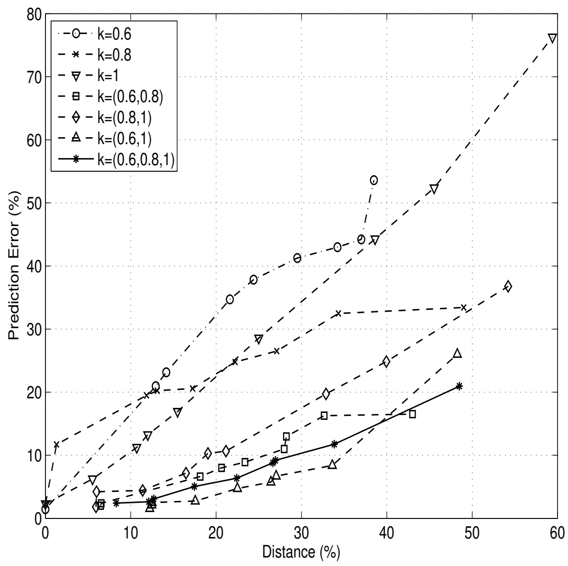

FIG. 12 – Prediction errors obtained using 1-control, 2-control and 3-control models

shows the disadvantage of using a 1-control model, with prediction errors of over 34% when the distance from the calibration dynamics increases over the 30%. As in the case $Re = 60$, the 2-control models give more accurate predictions than the 1-control

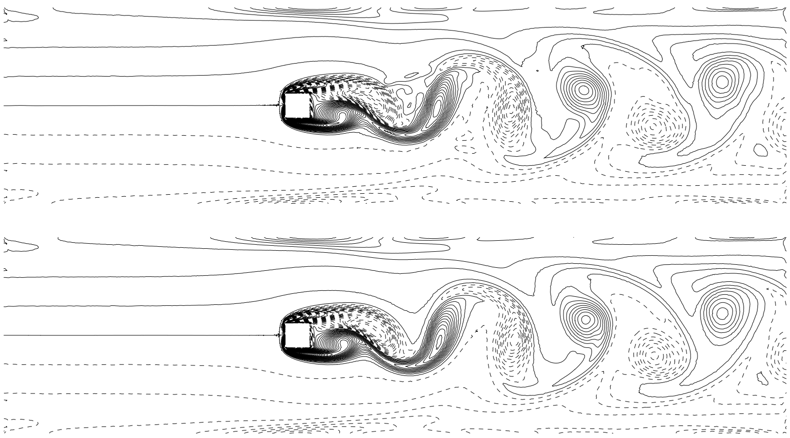

FIG. 13 – Model predicted vorticity field (top) and Navier-Stokes vorticity field at $t = T$ obtained with $\mathsf{K} = 0.1$. Positive (continuous lines) and negative (dashed lines) vorticity isolines

models. The lowest errors are obtained with the 2-control model ($\mathsf{K} = 0.6, \mathsf{K} = 0.1$). This observation suggests that, in model construction, an optimized a priori choice of the sampling points could be useful to obtain a more robust model. We note that in this case it was the model built to fit the highest and lowest values of K that gave the best result, and that adding a third intermediate control to the model ($\mathsf{K} = 0.8$) did not bring any improvement : the 3-control model gives more or less the same results.
In Fig. 13 we plot isolines of the vorticity at time $t = T$ for the flow obtained using $\mathsf{K} = 0.1$ as feedback gain (the first one in Fig.11). Time coefficients were obtained by integrating the 3-control model. The velocity field was then reconstructed using all the 60 coefficients and POD modes. The reconstructed vorticity is presented along with the vorticity obtained by running the Navier-Stokes equations with the test control law. The controls used to build the model were similar in the sense that they had a much stronger effect on the flow compared to the control obtained with $\mathsf{K} = 0.1$. We note that the model is able to accurately predict a flow snapshot and that the reconstructed flow is almost identical to that of the real flow.

5 Conclusions

The overall picture of reduced-order modeling that results from our study is the following. Given a control law, one can deduce a low-order model of the actuated flow by simply projecting the Navier-Stokes equations on POD modes. The coefficients of the quadratic model thus obtained are found by projection. However, a model constructed this way will show large time-integration errors even for the same control law used to generate the POD modes. Calibration can take care of that, in the sense that the model coefficients can be determined in order to match as closely as possible at least the

solution from which the POD modes are obtained. This might lead to a numerically stable model. However, this model is generally not at all robust, in the sense that the predictions for a slightly different configuration from that it was generated from, fails. A symptom of such lack of robustness is observed in the ill-posedness of the inverse problem : the matrices to be inverted are almost singular.
In order to get around this deficiency, we regularize the solution by adding a constraint to the minimization method used to solve the inverse problem. We ask that the coefficients of the polynomial expansion be close enough to those obtained by projection. This method allows to synthesize models that adequately simulate the flow in a small vicinity of the control law used to generate the solution database. However, the actual real improvement in robustness is obtained by spanning the solution manifold, i.e., by including several control laws in the inverse problem definition. By doing this, the results presented show that the models are able to predict dynamical behaviors that are far, in terms of an energy norm, from the cases included in the database. A consequence of such an additional regularization is that the matrices involved in the inverse problem solution become well conditioned.
Another important aspect of the method proposed, is that its cost is that of a matrix inversion, and that it does not scale with the number or the size of data sets used to build the model. Therefore it seems reasonable to envisage an automatic strategy to enrich the model by spanning the control space. In this respect, the technique proposed in [5] to distribute in an optimal way the points where to test the control space can help minimize the number of a priori simulations needed to build the model. For example, our results show that a model based on two controls might predict the effect of actuation laws not present in the data base, as precisely as a model based on three controls, if the two controls are appropriately placed.
In conclusion, the modeling we propose appears to be a viable approach to determine control strategies for those problems that because of their computational size cannot be treated in the framework of classical control theory.

Références

[1] M. Bergmann and L. Cordier. Optimal control of the cylinder wake in the laminar regime by trust-region methods and pod reduced-order models. *J. Comput. Phys.*, 2008. To appear.

[2] M. Bergmann, L. Cordier, and J.-P.Brancher. Optimal rotary control of the cylinder wake using proper orthogonal decomposition reduced-order model. *Physics of Fluids*, 17 :097101, 2005.

[3] M. Buffoni, S. Camarri, A. Iollo, E. Lombardi, and M. V. Salvetti. A non-linear observer for unsteady three-dimensional flows. *J. Comput. Phys.*, 227(4) :2626–2643, 2008.

[4] M. Buffoni, S. Camarri, A. Iollo, and M.V. Salvetti. Low-dimensional modelling of a confined three-dimensional wake flow. *Journal of Fluid Mechanics*, 569 :141–150, 2006.

[5] T. Bui-Thanh, K. Willcox, and O. Ghattas. *Parametric reduced-order models for probabilistic analysis of unsteady aerodynamic applications*. Collection of Technical Papers, Vol. 4. AIAA/ASME/ASCE/AHS/ASC, 2007.

[6] S. Camarri and F. Giannetti. On the inversion of the Kármán street in the wake of a confined square cylinder. *J. Fluid Mech.*, 574 :169–178, 2007.

[7] M. Couplet, C. Basdevant, and P. Sagaut. Calibrated reduced-order pod-galerkin system for fluid flow modelling. *J. Comput. Phys.*, 207(1) :192–220, 2005.

[8] B. Galletti, A. Bottaro, CH. Bruneau, and A. Iollo. Accurate model reduction of transient flows. *Europ. J. Mech. / B Fluids*, 26 :354–366, 2006.

[9] B. Galletti, C. H. Bruneau, L. Zannetti, and A. Iollo. Low-order modelling of laminar flow regimes past a confined square cylinder. *J.Fluid Mech.*, 503 :161–170, 2004.

[10] E. A. Gillies. Low-dimensional control of the circular cylinder wake. *J. Fluid Mech.*, 371 :157–178, 1998.

[11] W. R. Graham, J. Peraire, and K. Y. Tang. Optimal control of vortex shedding using low-order models. part i. *Int. J. Num. Meth. Eng.*, 44 :945–972, 1998.

[12] P.C. Hansen. *Rank-Deficient and Discrete Ill-Posed Problems : Numerical Aspects of Linear Inversion*. SIAM, Philadelphia, PA, USA, 1997.

[13] M. Hinze and S. Volkwein. Proper orthogonal decomposition surrogate models for nonlinear dynamical systems : Error estimates and suboptimal control. *Dimension Reduction of Large-Scale Systems*, pages 261–306, 2005.

[14] P. Holmes, J.L. Lumley, and G. Berkooz. *Turbulence, Coherent Structures, Dynamical Systems and Symmetry*. Cambridge University Press, 1996.

[15] A. Iollo, A. Dervieux, J. A. Désiéri, and S. Lanteri. Two stable pod-based approximations to the navier-stokes equations. *Comput. Visual. Sci.*, 3 :61–66, 2000.

[16] J. L. Lumley. The structure of inhomogeneous turbulent flows. In *Atmospheric Turbulence and Radio Wave Propagation,* edited by A. M. Yaglom and V. L. Tatarski, Nauka, Moscow, pages 166–178, 1967.

[17] X. Ma and G. E. Karniadakis. A low-dimensional model for simulating three-dimensional cylinder flow. *J. Fluid Mech.*, 458 :181–190, 2002.

[18] B.R. Noack, K. Afanasiev, M. Morzynski, G. Tadmor, and F. Thiele. A hierarchy of low-dimensional models for the transient and post-transient cylinder wake. *Comp. Meth. Appl. Mech. Eng.*, 497 :335 – 363, 2003.

[19] S.S. Ravindran. Optimal boundary feedback flow stabilization by model reduction. *Comp. Meth. Appl. Mech. Eng.*, 196 :2555–2569, 2007.

[20] D. Rempfer. On low-dimensional Galerkin models for fluid flow. *Theor. Comput. Fluid Dyn.*, 14 :75–88, 2000.

[21] L. Sirovich. Turbulence and the dynamics of coherent structures. Parts I,II and III. *Quarterly of Applied Mathematics*, XLV :561–590, 1987.

Centre de recherche INRIA Bordeaux – Sud Ouest
Domaine Universitaire - 351, cours de la Libération - 33405 Talence Cedex (France)

Centre de recherche INRIA Grenoble – Rhône-Alpes : 655, avenue de l'Europe - 38334 Montbonnot Saint-Ismier
Centre de recherche INRIA Lille – Nord Europe : Parc Scientifique de la Haute Borne - 40, avenue Halley - 59650 Villeneuve d'Ascq
Centre de recherche INRIA Nancy – Grand Est : LORIA, Technopôle de Nancy-Brabois - Campus scientifique
615, rue du Jardin Botanique - BP 101 - 54602 Villers-lès-Nancy Cedex
Centre de recherche INRIA Paris – Rocquencourt : Domaine de Voluceau - Rocquencourt - BP 105 - 78153 Le Chesnay Cedex
Centre de recherche INRIA Rennes – Bretagne Atlantique : IRISA, Campus universitaire de Beaulieu - 35042 Rennes Cedex
Centre de recherche INRIA Saclay – Île-de-France : Parc Orsay Université - ZAC des Vignes : 4, rue Jacques Monod - 91893 Orsay Cedex
Centre de recherche INRIA Sophia Antipolis – Méditerranée : 2004, route des Lucioles - BP 93 - 06902 Sophia Antipolis Cedex

Éditeur
INRIA - Domaine de Voluceau - Rocquencourt, BP 105 - 78153 Le Chesnay Cedex (France)
http://www.inria.fr
ISSN 0249-6399